Six Degrees-of-Freedom Prostate and Lung Tumor Motion MeasurementsUsing Kilovoltage Intrafraction Monitoring

Chen-Yu Huang,PhD,[*]Joubin NasehiTehrani,PhD,[*]Jin AunNg,PhD,[*,y] Jeremy Booth, PhD,[y,z] and Paul Keall, PhD[*]

**Radiation Physics Laboratory, Sydney Medical School*

[y]*Institute of Medical Physics, School of Physics, The University of Sydney*

[z]*Northern Sydney Cancer Centre, Royal North Shore Hospital, Sydney, New South Wales, Australia*

Reprint requests to: Paul Keall, PhD, Room 474, Blackburn Building D06, The University of Sydney, NSW 2006, Australia. Tel: (þ61) 2-9351- 3590; E-mail: paul.keall@sydney.edu.au

Funding support was received from the Australian National Health and Medical Research Council Australia Fellowship.

Conflict of interest: Drs Tehrani and Keall have filed a US patent application for this technology. The patent application is unlicensed.

Summary

Tumor intrafractional motion deteriorates radiation therapy efficacy. This report presents new data on prostate and lung tumor 6 degrees-of- freedom motion measured by kilovoltage intrafraction monitoring. Prostate and lung tumors rotated more than 5^{o} for about a third of time. Different patterns of rotation and respiration-induced tumor rotation were observed. This study is important for designing a 6 degrees-of-freedom tumor motion adaptation system to improve treatment conformality and reduce margins in radiation therapy.

Abstract

Purpose: Tumor positional uncertainty has been identified as a major issue that deteriorates the efficacy of radiation therapy. Tumor rotational movement, which is not well understood, can result in significant geometric and dosimetric inaccuracies. The objective of this study was to measure 6 degrees-of-freedom (6 DoF) prostate and lung tumor motion, focusing on the more novel rotation, using kilovoltage intrafraction monitoring (KIM).

Methods and Materials: Continuous kilovoltage (kV) projections of tumors with gold fiducial markers were acquired during radiation therapy for 267 fractions from 10 prostate cancer patients and immediately before or after radiation therapy for 50 fractions from 3 lung cancer patients. The 6 DoF motion measurements were determined from the individual 3-dimensional (3D) marker positions, after using methods to reject spurious and smooth noisy data, using an iterative closest point algorithm.

Results: There were large variations in the magnitude of the tumor rotation among different fractions and patients. Various rotational patterns were observed. The average prostate rotation angles around the left-right (LR), superior-inferior (SI), and anterior-posterior (AP) axes were 1.0 ± 5.0^{o}, 0.6 ± 3.3^{o}, and 0.3 ± 2.0^{o}, respectively. For 35% of the time, the prostate rotated more than 5^{o} about the LR axis, indicating the need for intrafractional adaptation during radiation delivery. For lung patients, the average LR, SI, and AP rotation angles were 0.8 ± 4.2^{o}, -0.8 ± 4.5^{o}, and 1.7 ± 3.1^{o}, respectively. For about 30% of the time, the lung tumors rotated more than 5^{o} around the SI axis. Respiration-induced rotation was detected in 2 of the 3 lung patients.

Conclusions: The prostate and lung tumors were found to undergo rotations of more than 5^{o} for about a third of the time. The lung tumor data represent the first 6 DoF tumor motion measured by kV images. The 6 DoF KIM method can enable rotational and translational adaptive radiation therapy and potentially reduce treatment margins.

Introduction

Thoracic, abdominal, and pelvic tumors are not static inside the human body; they undergo translational and rotational motion. Uncorrected tumor movement can cause the tumor to become misaligned with the radiation beam, compromising cancer control and increasing normal tissue toxicity. Methods of correcting for intrafractional tumor translation have previously been reported (1-3). However, increasing evidence suggests that intrafractional tumor motion corrections should be applied not only to tumor translation but also to rotation (4, 5). It has previously been shown that a small off-center rotation of an elongated target can result in a displacement of 13% of the target beyond the planning tumor volume (PTV) (4) and that uncorrected prostate tumor rotations of 15^{o} can result in a 12% underdose to the tumor (6). As tighter PTV margins are applied and fractionation regimens are shortened (largely owing to translational compensation), factors such as tumor rotation will become the dominant concern for accurate tumor targeting. The aim of this study was to quantify the intrafractional tumor rotation in patients with prostate and lung cancer and to understand the requirements for a real-time tumor rotation adaptation system.

Intrafractional tumor rotations of the prostate have previously been measured using electromagnetic tracking (Calypso transponder) (5, 7) and MV images with gold fiducial markers (8). Each study reported similar magnitudes of prostate rotation, with the predominant rotation being about the LR axis. The only previous study regarding lung tumor rotation reported slow breathing measurements with magnetic resonance imaging (MRI), wherein a maximum rotation of more than 45^{o} was observed (9). Novel monitoring methods and further investigation into the intrafractional tumor rotation are needed.

A recently developed method that is capable of monitoring real-time tumor motion is kilovoltage intrafraction monitoring (KIM) (10). KIM demonstrated high accuracy under clinical conditions, and a comparison between KIM and Calypso was summarized by Ng et al (11). The current work extends the KIM system by including tumor rotation monitoring. Tumor rotation calculations using KIM have been previously carried out by the iterative closest point (ICP) algorithm but have been applied to only 1 fraction of each of 10 prostate cancer patients (12). The purpose of this study was to perform 6 degrees-of-freedom (DoF) prostate and lung tumor motion measurements using KIM.

Methods and Materials

Rotation measurement

An overview of the 6 DoF monitoring method is shown in Figure 1. Briefly, a series of 2-dimensional (2D) x-ray projections are acquired during radiation therapy by a single kV imager (Fig. 1A and 1B). Our in-house software will segment the gold fiducial markers (Fig. 1C) and reconstruct their 3- dimensional (3D) positions using the maximum likelihood estimation of a 3D probability density function (Fig. 1D) (10). With the marker 3D position information, tumor rotation and translation are calculated by the ICP algorithm (12, 13) (Fig. 1E). The ICP algorithm performs matching for each fiducial marker based on the nearest neighbor algorithm and generates a rotation matrix and translation vector (14). Rotation angles about 3 orthogonal axes (LR, SI, AP) were determined with the pivot set at the centroid of the 3 markers. In this study, rotation angles were calculated between the current time and a reference time at the beginning of each fraction to determine intrafraction rotation and also at the beginning of treatment to quantify the interfraction and intrafraction rotation. Inasmuch as tumor translation has been much more widely studied, and the patient database used in this study have been published for the prostate (11) and the lung (15), the results here focus on the rotation measurements.

Patient database

In the KIM prostate tumor motion study, 10 prostate cancer patients had 3 cylindrical gold fiducial markers (1 x 3 mm) implanted and treated with fractionated double-arc volumetric modulated arc therapy (11). Continuous kV images were acquired using a kV imager (OBI, Varian) when the treatment beam was on. The exposure parameters were 125 kVp, 80 mA,and 13 ms. To reduce patient dose, a field size of 6 x 6 cm^2 was chosen as the minimum necessary to cover the marker positions from all gantry angles. The image frequency was 5 Hz or 10 Hz depending on the desired image quality. The imaging dose from KIM was quantified to be 185 mGy over the course of a prostate intensity- modulated radiation therapy for 120 kV (1.04 mAs) imaging at 1 Hz, a small portion of the total treatment dose (16). In a 7-lung tumor motion study, 4 patients had 3 markers (3 patients) or 4 markers (1 patient) implanted. However, 2 of these patients had 2 markers implanted within close proximity, 1 with 3 markers and 1 with 4 markers. Differentiation between these markers was not possible (15). Therefore, 1 of the 3-marker patients was excluded, leaving 3 patients remaining. No patients were excluded for image quality; however, 11 of the 61 fractions were excluded because of poor image quality. The tumor location in 2 patients was the right hilum, and in the third it was the left lower lobe. Fiducial gold coils (0.35 10 or 20 mm) were implanted into the lung. For each of the treatment fractions, 8-minute kV imaging sequences, corresponding to the duration of a typical radiation treatment, were taken by the kV imager at 10 Hz immediately before or after treatment. The exposure parameters were 125 kVp, 20 mA, and 20 ms per projection. We estimate the lung imaging dose (more projections, less dose per projection) for a 6 x 6 cm^2 field size (reducing the field size to only show the lung markers) at 1 Hz to also be approximately 190 mGy.

Data acceptance and noise filtering methods

The ICP algorithm takes individual 3D marker position as input. However, the accuracy of the marker coordinates is subject to variable image quality, the accuracy of the 2D marker segmentation, and the 3D reconstruction algorithm. To improve marker position fidelity for each fraction before calculating tumor rotation, we implemented 4 methods to reject spurious and smooth noisy data. Each step is briefly described here.

Correlation

In the marker segmentation step, marker position was determined as the position with the highest normalized cross-correlation between the template and the projection image (17). Data are prone to noise if the correlation is low.

In this study, the correlation threshold value was set at 0.3 for prostate patients (0.3% of data removed) and 0.4 for lung patients (8.1% removed).

Despiking

A phase-space thresholding method (18) was used to remove spikes from the marker trajectory. Normally, valid data are tightly clumped within an ellipsoid cloud in phase space (3D plots of velocity, u, and approximations of acceleration and jerk, Δu and $\Delta^2 u$, respectively). Spikes or the points outside the phase-space thresholds are iteratively removed. A universal threshold parameter $\sqrt{2 \ln n}$ Was applied to the lung data series (7.3% removed), and 2 times the universal threshold was applied to the prostate data series (0.6% removed).

Rigidity

The area defined by vertices of the triangle formed by the 3 fiducial markers was calculated over time. Tumor rigidity was calculated based on the change in the area of the triangles. The data were regarded as being false positive if the change in the triangle area was beyond a set threshold. For the prostate, the rigidity threshold was set as 5% (0.1% removed). For lung patients, the rigidity threshold was set at 10% because larger changes are expected from respiratory induced motion in the lung (0.1% removed).

L1 trend filtering

The L1 trend filtering method was used to smooth the original noisy data series. The L1 filtering method can be used for real-time trend filtering with a smaller filter window size. It generates trend estimates that are smooth in the sense of being piecewise linear. For a given time series y_t, t = 1,……,n with an underlying slowly varying trend x_t, L1 chooses the trend estimate as the minimizer of the weighted sum objective function

$$\left(\tfrac{1}{2}\right)\sum_{t=1}^{n}(y_t - x_t)^2 + \lambda\sum_{t=2}^{n-1}|x_{t-1} - 2x_t + x_{t+1}| \qquad (19).$$

A regularization parameter l controls the tradeoff between the smoothness of the trend and the size of the residual. In this work, λ was set to 0.1.

Sensitivity analysis

Each of the 4 steps involves setting a parameter. The final values were determined heuristically with the goal of maintaining the maximum amount of original data while removing obvious noise and spurious results. A sensitivity analysis was performed by increasing and decreasing the parameter values in each of the 4 steps by at least ±33%. Even with these large changes, the mean value changed by ≤0.1°and standard deviation (SD) ≤0.15°, indicating that the mean and SD are not sensitive to the selection of the parameters. The differences lie in the amount of data that were removed (≤ 34%) and the values of the maximal and minimal rotation.

Results

Prostate and lung tumor rotation

Continuous prostate and lung rotation was calculated. Table 1 lists the mean and SD of intrafraction and interfraction for prostate and lung from this study and also compares the current results with those of previous studies (7-9, 12, 20, 21).
For prostate cancer patients, the SD of interfractional and intrafractional rotation was 5.5°, 3.0°, and 2.0° about the LR, SI, and AP axes, respectively, which was larger than intrafractional rotation. Prostate rotation about the LR axis was the most predominant of the 3 rotation axes and was in agreement with previous published results. For lung cancer patients, the SD of interfractional and intrafractional rotation was 2.9°, 4.6° and 3.0° about the LR, SI, and AP axes, respectively. Rotation around the SI axis was the major rotation among all 3 axes.
The prostate and lung tumor interfraction and intra- fraction translation and rotation distributions are shown in the matrix diagonal of Figure 2. The prostate rotated more than 5° about the LR axis for more than 35% of the time, highlighting the desirability of applying tumor rotational corrections during radiation delivery. Lung tumors were found to rotate more than 5° about the SI axis for about 30% of the time. Prostate and lung tumor rotations of more than 30° were observed, but the exact maximal rotation angle depends strongly on the data acceptance and noise filtering methods applied. If stricter thresholds or higher λ values in the L1 filtering method were applied, more data would be rejected, and the trajectory would become smoother, thus resulting in a reduced maximum rotation angle.

The kV images of a rotated prostate and lung were selected to show intrafractional tumor rotation in Figure 3. The images are of the same prostate and lung taken at the same gantry angle at different time points.

Rotation patterns

Tumors were observed to undergo variable rotational behavior over time among the patients. Rotation analogues of the translational motion types described initially by Kupelian et al (3) for Calypso and Ng et al (11) for KIM were observed. These classifications are important for designing the rotation adaptation system because the management of each pattern of rotation is different. Ex- amples of these rotation patterns are shown in Figure 4 for prostate and lung.
The magnitude of prostate and lung tumor rotation also differed greatly from fraction to fraction and patient to patient. The dosimetric effect of tumor rotation is therefore expected to be significantly larger for a given subgroup of patients. Of particular note are tumors within the class of lung persistent rotation (Fig. 4), in which >6 of LR rotation was observed for most of the treatment time, indicating a large geometric uncertainty.

Respiratory component in lung tumor rotation

From the lung rotation traces in Figure 4, respiratory cycles could be readily observed. To further analyze the effect of breathing in lung tumor rotation, the power spectrum cor- responding to SI rotation was plotted for each patient.
Peaks at ~0.3 Hz were observed in the power spectrum for 2 lung patients (Fig. 5); 0.3 Hz is equivalent to a signal cycle of every 3.3 seconds, which is a typical respiratory cycle for patients. However, this phenomenon was not observed in patient 2, which may be a result of the tumor location (left lower lobe vs right hilum) and could also be a result of atelectasis experienced by the patient during the treatment period (15). Interestingly, no predominant peaks were observed around 0.5 to 1 Hz, indicating that the cardiac cycle did not introduce tumor rotation for these

patients.

Correlation of 6 DoF tumor motion

Pearson linear correlation coefficients were calculated be- tween all sets of tumor 6 DoF motion for the prostate and lung patients separately (Fig. 2). Histograms of each 3 DoF translation (mm) and 3 DoF rotation (^{o}) are along the matrix diagonal; scatter plots of variable pairs appear off-diagonal with the unit of millimeter.
High correlations were observed between the prostate AP translation and the SI translation (0.89), between the lung tumor AP and the SI translation (0.63), and between the AP translation and rotation (0.62). These 6 DoF tumor motion correlation values are population based, and the correlations are different for individual patients.

Discussion

In this report, we describe 6 DoF tumor motion measurements using the KIM method, focusing on the more novel rotational motion results. Tumor rotation about 3 axes was calculated by determining the position of gold fiducial markers in successive 2D kV images acquired continuously during treatment or before or after treatment. This method is widely applicable because the majority of radiation therapy linear accelerators purchased today incorporate gantry-mounted kV imagers. In addition, the implantation of gold fiducial markers is the current clinical standard of care for prostate patient setup before radiation therapy (22). The tumor motion monitoring and adaptation based on the KIM method can be performed at no additional cost in terms of linac hardware; however, implanting lung fiducial markers does require additional procedures and may introduce side effects.

We show that for both prostate and lung tumors, the SDs of interfractional and intrafractional rotation are larger than intrafractional rotation because of greater day-by-day tumor position variation. Our results also demonstrate that intrafractional tumor rotation during radiation therapy can be unpredictable, with rotation patterns ranging greatly from small rotation, continuous rotation, transient rotation, persistent rotation, and high-frequency rotation to erratic rotation, or a combination thereof. Tumor intrafractional motion caused by the patient's spontaneous rectum and bladder filling, flatulence, muscle contractions, and breathing is hard to exclude. Thus, the adaptation to intrafractional tumor motion is best handled by modern tracking techniques, such as dynamic multileaf collimator tracking, Cyberknife, and Gimbaled system (23).

Diaphragm (24) and lung tumor rotation (25) was observed in 4-dimensional computed tomography but not quantified. Given the complexity of lung motion, we present the first attempt to demonstrate high-frequency respiratory-induced rotation from general lung movement. The rotation power spectrum peak at 0.3 Hz (or 3.3 seconds), which is a typical breathing cycle, indicates that there is a respiratory component to lung tumor rotational movement. Our 50 fractions of images show that the strength of the respiratory signal in rotation appears to depend on thetumor position within the lung, although a strong conclusion would need more patient data; only 3 patients are included in this analysis. The effect of marker position deformation was accounted for by a data acceptance method: rigidity in this study. Tumor rigidity was calculated based on the change in the area of the triangles. We showed that for intrafractional rotation, less than 0.1% of data was removed by rigidity thresholding.

The KIM measured prostate rotation is similar to the values measured by other methods (Table 1). The lung tumor rotation result is different from the MRI measured result, and this could be due to the different measurement methods. The KIM rotation calculation method is highly

accurate. First, the KIM method achieved 0.46 mm accuracy in the prostate cancer patient clinical trial (11). Second, the root mean square error of the ICP algorithm in a simulation study has previously been reported as 0.004^{o} (12). However, the present study was affected by the kV image quality. Markers are generally more difficult to identify in kV images taken through the lateral side of a patient, and their identification is especially difficult in larger patients because of increased photon scattering. Furthermore, for certain lung patients, the spine, medical wires, and other objects can partially obstruct the radiation beam and cause marker segmentation problems at certain projection angles. With extra image quality enhancement steps, the marker-based localization method can be greatly improved.

Monitoring tumor rotation is the first step toward real-time rotation adaptive radiation therapy. Independent studies have shown that considering tumor rotation reductions in the treatment margin by 2 to 3 mm is possible (20, 26). There are higher accuracy requirements for the emerging stereotactic body radiation therapy (SBRT), wherein the radiation treatment is hypofractionated and each fraction delivers a higher dose of radiation over a longer period of time (27). The ability to track target tumor motion by considering not only translation but also rotation could potentially address the high precision requirement of SBRT.

Conclusions

This study examined the use of a gantry-mounted kV imager to measure 6 DoF tumor motion by KIM. The lung tumor data represent the first 6 DoF motion measured by kV images. The prostate tumor data represent the most comprehensive 6 DoF motion measurements with KIM. In both prostate and lung cancer patients, tumors were found to undergo rotations of more than 5° for about a third of the total treatment time. Various of rotation patterns were observed, with LR rotation for prostate and SI rotation for lung patients having the highest magnitude. In as much as gantry-mounted kV imagers are present in most new cancer radiation therapy systems, there is potential for the technique to be widely used. The 6 DoF KIM method can enable rotational and translational adaptive radiation therapy and potentially reduce treatment margins.

Acknowledgments The authors thank Drs Thomas Eade and Andrew Kneebone, Geoff Hugo, and Ms Shufei Chen for providing the prostate and lung kV projections; Chun-Chien Shieh for assistance with data analysis; Jonathan Yeow for proofreading; Heinrich Deutschmann for useful discussions; and Per Poulsen and Walther Fledelius for developing the 3-dimensional kilovoltage intrafraction monitoring code.

References

1. Sawant A, Smith RL, Venkat RB, et al. Toward submillimeter accu- racy in the management of intrafraction motion: The integration of real-time internal position monitoring and multileaf collimator target tracking. *Int J Radiat Oncol Biol Phys* 2009;74:575-582.
2. Keall PJ, Colvill E, O'Brien R, et al. The first clinical implementation of electromagnetic transponder-guided mlc tracking. *Med Phys* 2014; 41:020702.
3. Kupelian P, Willoughby T, Mahadevan A, et al. Multi-institutional clinical experience with the calypso system in localization and continuous, real-time monitoring of the prostate gland during external radiotherapy. *Int J Radiat Oncol Biol Phys* 2007;67:1088-1098.
4. Amro H, Hamstra DA, McShan DL, et al. The dosimetric impact of prostate rotations during electromagnetically guided external-beam radiation therapy. *Int J Radiat Oncol Biol Phys* 2013;85:230-236.
5. Wu J, Ruan D, Cho B, et al. Electromagnetic detection and real-time dmlc adaptation to target rotation during radiotherapy. *Int J Radiat Oncol Biol Phys* 2012;82:e545-e553.
6. Rijkhorst E-J, Lakeman A, Nijkamp J, et al. Strategies for online organ motion correction for intensity-modulated radiotherapy of prostate cancer: Prostate, rectum, and bladder dose effects. *Int J Radiat Oncol Biol Phys* 2009;75:1254-1260.
7. Olsen JR, Noel CE, Baker K, et al. Practical method of adaptive radiotherapy for prostate cancer using real-time electromagnetic tracking. *Int J Radiat Oncol Biol Phys* 2012;82:1903-1911.
8. Aubry J-F, Beaulieu L, Girouard L-M, et al. Measurements of intrafraction motion and interfraction and intrafraction rotation of

prostate by three-dimensional analysis of daily portal imaging with radiopaque markers. *Int J Radiat Oncol Biol Phys* 2004;60: 30-39.
9. Plathow C, Schoebinger M, Fink C, et al. Quantification of lung tumor volume and rotation at 3d dynamic parallel MR imaging with view sharing: Preliminary results. *Radiology* 2006;240:537-545.
10. Poulsen PR, Cho B, Keall PJ. Real-time prostate trajectory estimation with a single imager in arc radiotherapy: A simulation study. *Phys Med Biol* 2009;54:4019-4035.
11. Ng JA, Booth JT, Poulsen PR, et al. Kilovoltage intrafraction moni- toring for prostate intensity modulated arc therapy: First clinical re- sults. *Int J Radiat Oncol Biol Phys* 2012;84:e655-e661.
12. Tehrani JN, O'Brien R, Poulsen PR, et al. Real-time estimation of prostate tumor rotation and translation with a kv imaging system based on an iterative closest point algorithm. *Phys Med Biol* 2013;58:8517.
13. Chen Y, Medioni G. Object modeling by registration of multiple range images. *IEEE Int Conf Robot Autom* 1991;3:2724-2729.
14. Cover T, Hart P. Nearest neighbor pattern classification. *IEEE Trans Infor Theory* 1967;13:21-27.
15. Roman NO, Shepherd W, Mukhopadhyay N, et al. Interfractional positional variability of fiducial markers and primary tumors in locally advanced non-small-cell lung cancer during audiovisual biofeedback radiotherapy. *Int J Radiat Oncol Biol Phys* 2012;83: 1566-1572.
16. Crocker JK, Ng JA, Keall PJ, et al. Measurement of patient imaging dose for real-time kilovoltage x-ray intrafraction tumour position monitoring in prostate patients. *Phys Med Biol* 2012;57:2969-2980.
17. Fledelius W, Worm E, Elstrom UV, et al. Robust automatic segmen- tation of multiple implanted cylindrical gold fiducial markers in cone- beam CT projections. *Med Phys* 2011;38:6351-6361.
18. Goring DG, Nikora VI. Despiking acoustic doppler velocimeter data. *J Hydraul Eng* 2002;128:117-126.

19. Kim S-J, Koh K, Boyd S, et al. L1 trend filtering. *Siam Review* 2009; 51:339-360.
20. Li JS, Jin L, Pollack A, et al. Gains from real-time tracking of prostate motion during external beam radiation therapy. *Int J Radiat Oncol Biol Phys* 2009;75:1613-1620.
21. Deutschmann H, Kametriser G, Steininger P, et al. First clinical release of an online, adaptive, aperture-based image-guided radio- therapy strategy in intensity-modulated radiotherapy to correct for inter- and intrafractional rotations of the prostate. *Int J Radiat Oncol Biol Phys* 2012;83:1624-1632.
22. Shirato H, Harada T, Harabayashi T, et al. Feasibility of insertio- n/implantation of 2.0-mm-diameter gold internal fiducial markers for precise setup and real-time tumor tracking in radiotherapy. *Int J Radiat Oncol Biol Phys* 2003;56:240-247.
23. Kamino Y, Miura S, Kokubo M, et al. Development of an ultrasmall c- band linear accelerator guide for a four-dimensional image-guided radiotherapy system with a gimbaled x-ray head. *Med Phys* 2007;34: 1797-1808.
24. Liu HH, Balter P, Tutt T, et al. Assessing respiration-induced tumor motion and internal target volume using four-dimensional computed tomography for radiotherapy of lung cancer. *Int J Radiat Oncol Biol Phys* 2007;68:531-540.
25. Wang Y, Bao Y, Zhang L, et al. Assessment of respiration-induced motion and its impact on treatment outcome for lung cancer. *Bio- med Res Int* 2013;2013:872739.
26. Thomas SJ, Ashburner M, Tudor GSJ, et al. Intra-fraction motion of the prostate during treatment with helical tomotherapy. *Radiother Oncol* 2013;109:482-486.
27. Konski AA, Wallner PE, Harris EER, et al. Stereotactic body radio- therapy (SBRT) for primary management of early-stage, low-interme- diate risk prostate cancer: Report of the ASTRO Emerging Technology Committee. Available at: https://www.astro.org/uploadedFiles/Main_ Site/Clinical_Practice/Best_Practices/SBRTreport.pdf. Published Sep- tember 19, 2008. Accessed November 13, 2014.

Table 1 Prostate and lung tumor rotation measurements of this study along with previously published studies

Study	Tumor site [no. of patients]	Measurement method	Reference image	Rotation angle, °		
				LR	SI	AP
This study	Prostate [10]	Gold marker with kV image	Intrafraction	0.0 ± 1.8	0.1 ± 1.0	0.2 ± 0.8
			Interfraction and intrafraction	0.7 ± 5.5	0.8 ± 3.0	0.1 ± 2.0
Olsen et al (7)	Prostate [15]	Calypso	Simulation CT	5.7 ± 5.0	2.0 ± 2.0	1.6 ± 1.0
Li et al (20)	Prostate [29]	Calypso	First treatment	1.5 ± 5.2	0.4 ± 1.7	0.8 ± 1.6
Aubry et al (8)	Prostate [7]	Gold marker with MV image	Compare 2 reconstructions in the same fraction	−0.5 ± 5.8	0.5 ± 3.8	0.4 ± 2.0
Deutschmann et al (21)	Prostate [39]	Gold marker with MV image	Intrafraction	2.5 ± 2.3	2.3 ± 2.0	2.4 ± 2.1
Tehrani et al (12)	Prostate [10]	Gold marker with kV image	Intrafraction	0.1 ± 2.3	0.2 ± 0.9	−0.01 ± 0.7
This study	Lung [3]	Gold marker with kV image	Intrafraction	−0.4 ± 2.6	−0.3 ± 3.0	0.0 ± 1.8
			Interfraction and intrafraction	1.0 ± 2.9	−0.9 ± 4.6	0.5 ± 3.0
Plathow et al (9)	Lung [5]	MRI	Maximum value from single session slow breathing measurement with maximal expiration	25.4 ± 13.4	18.9 ± 11.8	23.1 ± 8.5

Abbreviations: AP = anterior-posterior; CT = computed tomography; LR = left-right; MRI = magnetic resonance imaging; SI = superior-inferior. For intrafraction rotation of this study, the first image of each fraction was used as the reference. For interfraction and intrafraction rotation of this study, the first image of the first treatment fraction was used as the reference.

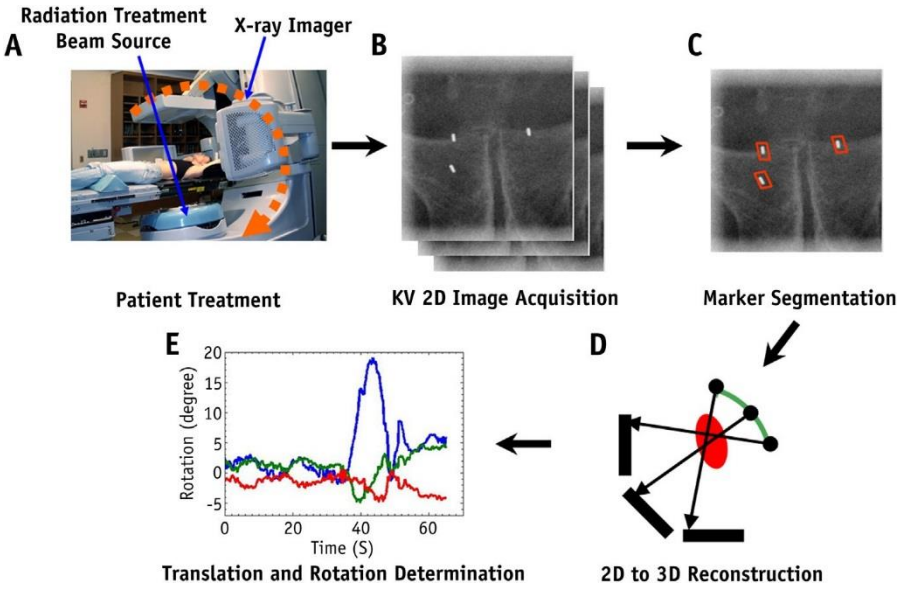

Fig. 1. Overview of the 6 degrees-of-freedom tumor motion monitoring strategy. (A) Patient undergoing radiation therapy. (B) kV 2-dimensional (2D) images are acquired continuously during radiation therapy. (C) Gold fiducial markers on each kV image are segmented. (D) Marker 3-dimensional (3D) positions are reconstructed. (E) Tumor rotation and translation (6 DoF) motion are calculated.

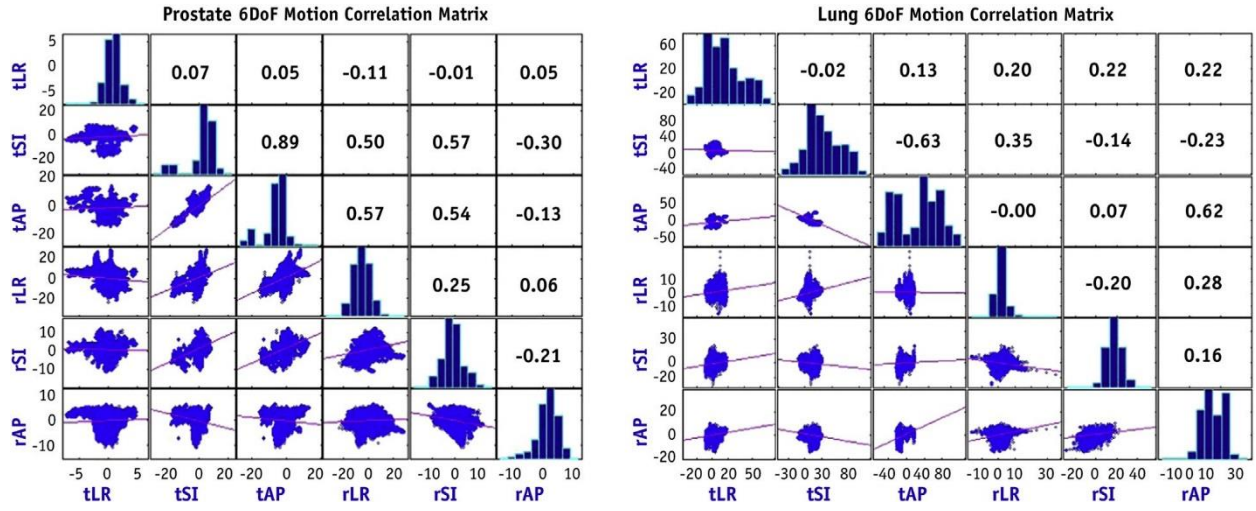

Fig. 2. Correlation matrix of prostate (left) and lung (right) 6 degrees-of-freedom motion. tLR, tSI, and tAP denote LR, SI, and AP translation, respectively; rLR, rSI, and rAP denote LR, SI, and AP rotation, respectively. Histograms of each 3 DoF translation (mm) and 3 DoF rotation (^{o}) are along the matrix diagonal. The slopes of the least-squares reference lines in the scatterplots are equal to the displayed correlation coefficients

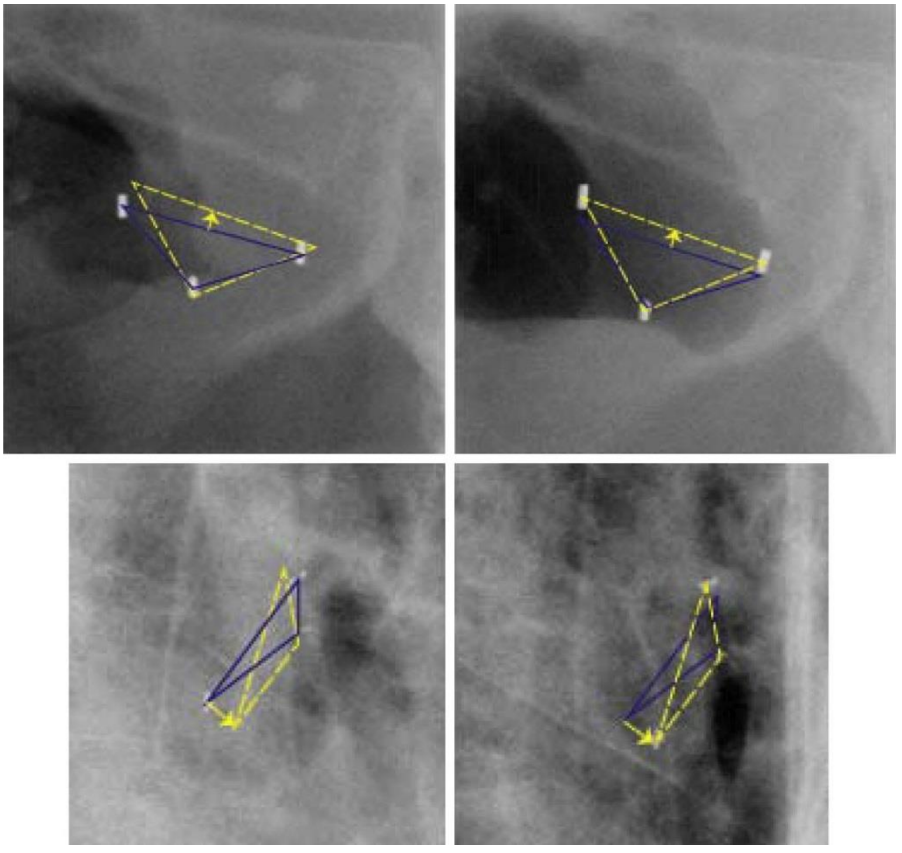

Fig. 3. kV images of a rotated prostate and lung. Compared with the initial position (left) the prostate has rotated −15.2°, 0.8°, and 0.9° about the left-right, superior-inferior, and anterior-posterior axes (upper right), and the lung tumor has rotated 0.9°, −12.3°, and −4.1° (lower right). Blue triangles represent the tumor initial position. Yellow arrows and dashed triangles denote the rotation direction and the rotated tumor positions.

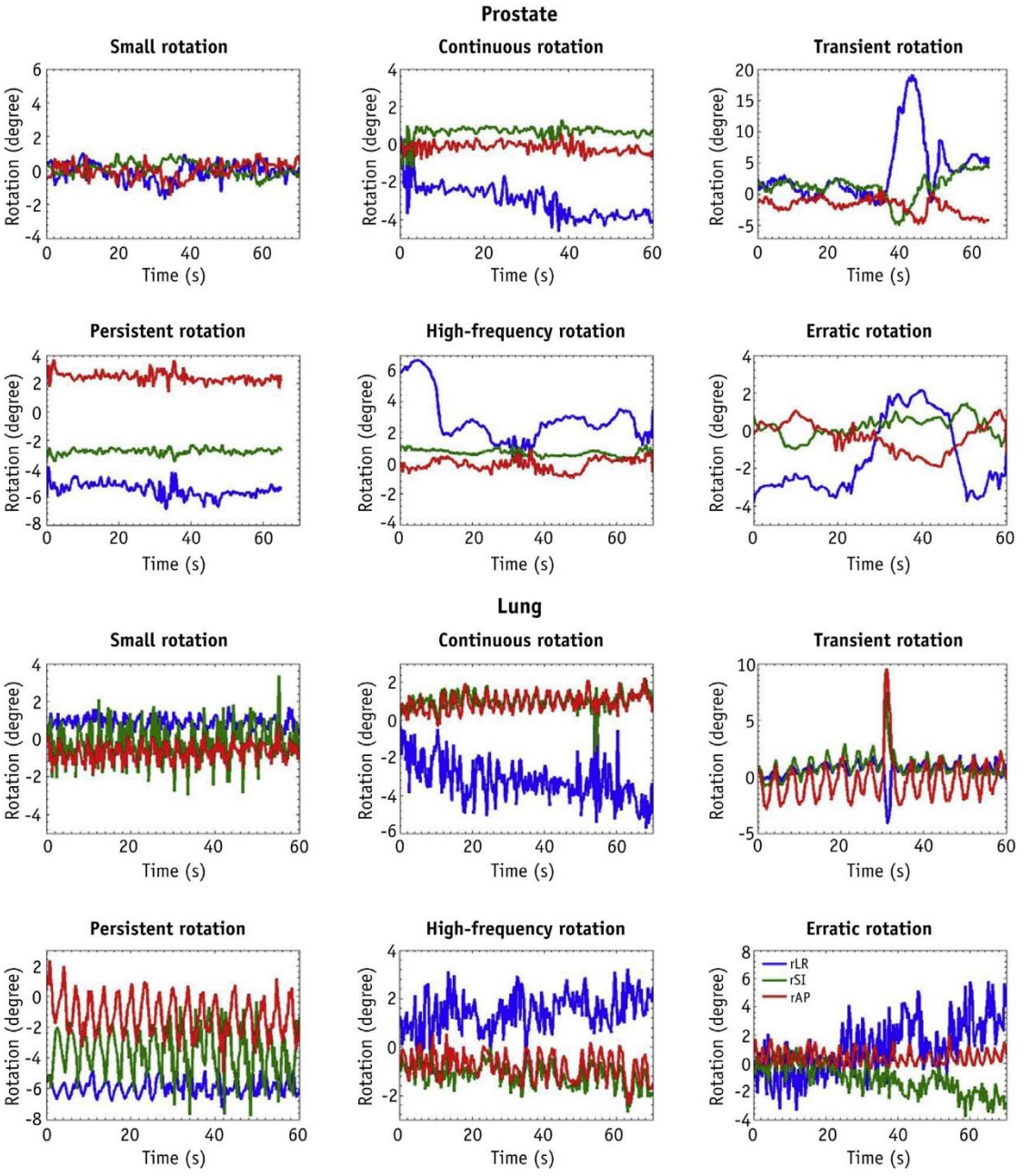

Fig. 4. Examples of observed intrafractional prostate (upper 2 rows) and lung (lower 2 rows) tumor rotation pattern. The left-right (red), superior-inferior (green), and anterior-posterior (blue) rotations are shown.

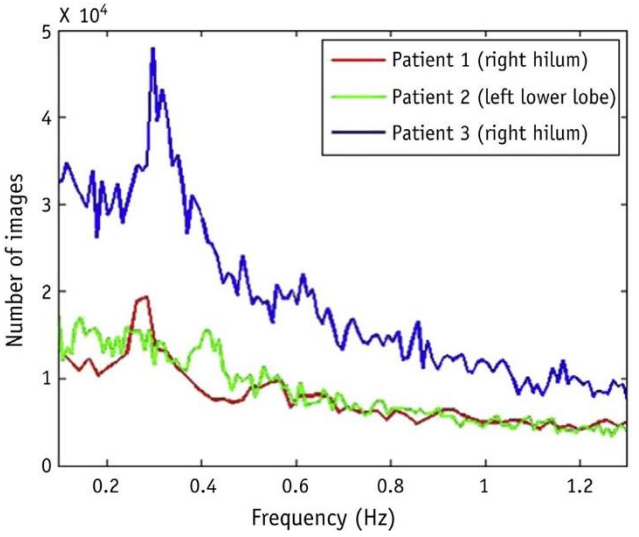

Fig. 5. Power spectrum of lung tumor superior-inferior rotation.